

1 **Study of electron spectral diffusion process under DNP conditions by**
2 **ELDOR spectroscopy focusing on the ^{14}N Solid Effect**

3
4 Marie Ramirez Cohen, Akiva Feintuch, Daniella Goldfarb*, Shimon Vega*

5 ¹Department of Chemical Physics, Weizmann Institute of Science, Rehovot, Israel.

6 *Corresponding authors: Daniella Goldfarb (daniella.goldfarb@weizmann.ac.il),
7 Shimon Vega (shimon.vega@weizmann.ac.il)

8 **Abstract** Electron spectral diffusion (eSD) plays an important role in solid state,
9 static DNP with polarizers having in-homogeneously broadened EPR spectra, such as
10 nitroxide radicals. It affects the electron spin polarization gradient within the EPR
11 spectrum during microwave irradiation and thereby determines the effectiveness of the
12 DNP process via the so called indirect cross effect (iCE) mechanism. The electron
13 depolarization profile can be measured by electron-electron double resonance
14 (ELDOR) experiments and a theoretical framework for deriving eSD parameters from
15 ELDOR spectra and employing them to calculate DNP profiles has been developed.
16 The inclusion of electron depolarization arising from the ^{14}N Solid Effect (SE) has not
17 yet been taken into account in this theoretical framework and is the subject of the
18 present work. The ^{14}N SE depolarization was studied using W-band ELDOR of a 0.5
19 mM TEMPOL solution, where eSD is negligible, taking into account the hyperfine
20 interaction of both ^{14}N and ^1H nuclei, the long microwave irradiation applied under
21 DNP conditions and electron and nuclear relaxation. The results of this analysis were
22 then used in simulations of ELDOR spectra of 10 and 20 mM TEMPOL solutions,
23 where eSD is significant using the eSD model and the SE contributions were added ad-
24 hoc employing the ^1H and ^{14}N frequencies and their combinations, as found from the
25 analysis of the 0.5 mM sample. This approach worked well for the 20 mM solution
26 where a good fit for all ELDOR spectra recorded along the EPR spectrum was obtained
27 and the inclusion of the ^{14}N SE mechanism improved the agreement with the
28 experimental spectra. For the 10 mM solution, simulations of the ELDOR spectra
29 recorded along the g_z position gave a lower quality fit than for spectra recorded in the
30 center of the EPR spectrum. This indicates that the simple approach we used to describe
31 the ^{14}N SE is limited when its contribution is relatively high as the anisotropy of its
32 magnetic interactions was not considered explicitly.

33

1 Introduction

2 It has been recently recognized that electron spectral diffusion (eSD) plays a significant
3 role in dynamic nuclear polarization (DNP) under static conditions(Hovav et al., 2015a;
4 Leavesley et al., 2017). It affects the electron spin polarization gradient within the EPR
5 spectrum as a consequence of microwave irradiation and thereby determines the
6 effectiveness of the DNP process via the so called indirect cross effect (iCE)
7 mechanism(Hovav et al., 2015a). This is particularly relevant in the case of nitroxide
8 radicals, the EPR spectra of which are in-homogeneously broadened in frozen solutions,
9 at concentrations of 20-40 mM used in DNP applications. Hovav *et al* (Hovav et al.,
10 2015b, 2015a), Siaw *et al*(Siaw et al., 2014) and Shimon *et al*(Shimon et al., 2012,
11 2014) observed that during constant microwave (MW) irradiation there exists an
12 optimal radical concentration that leads to a maximum in the DNP enhancement. At
13 this concentration the inter-electron spin dipolar interaction is sufficiently strong to
14 generate a polarization gradient that favors an efficient iCE enhancement mechanism,
15 while at higher concentrations the spectral diffusion saturates large parts of the EPR
16 spectrum and spin temperature effects can be expected(Caracciolo et al., 2016; Kundu
17 et al., 2018a, 2018b). To monitor directly the electron depolarization during MW
18 irradiation, Hovav *et al*(Hovav et al., 2015b) measured the ELDOR signals of frozen
19 TEMPOL solutions, under static DNP conditions, as a function of TEMPOL
20 concentration, sample temperature and MW irradiation time. Furthermore, they
21 developed a model (called the eSD model) that describes the depolarization process.
22 This model is based on rate equations for the electron polarizations along the EPR
23 spectrum, taking into account an exchange process between polarizations, in addition
24 to the saturation effects of the MW irradiation and the spin-lattice relaxation. This eSD
25 model introduces a fitting parameter Λ^{eSD} that defines the strength of the polarization
26 exchange rate leading to the spectral diffusion within the EPR spectrum. Using this eSD
27 model, experimental ELDOR spectra could be satisfactorily simulated and thus provide
28 a feasible description of the eSD process. Subsequently, it was demonstrated that once
29 the polarization gradient within the EPR spectrum has been determined via the eSD
30 model simulations, the lineshape of the associated DNP spectrum could be reproduced
31 taking into account the polarization differences between all electron pairs satisfying the
32 CE condition(Hovav et al., 2015a). This approach was also implemented by Leavesley
33 *et al*, (Leavesley et al., 2017) when they explored the eSD process and its influence on

1 the DNP efficiency at a magnetic field of 7 T. They also considered the effects of
2 variations in the radical concentration, temperature and MW power on the ^1H -DNP
3 spectra. Furthermore, Kundu *et al.* used the eSD model to quantify the dependence of
4 the electron polarization exchange parameter Λ^{eSD} on radical concentration and
5 temperature⁷.

6 To justify the rather phenomenological eSD model, Kundu *et al.*(Kundu et al., 2018a,
7 2018b) performed quantum mechanical based calculations of the spin evolution and
8 associated EPR spectra of the electron spins in dipolarly coupled small spin systems
9 under DNP conditions. In the case of weak dipolar coupling constants and adding cross
10 relaxation(Hwang and Hill, 1967; Kessenikh et al., 1964) to the ELDOR calculations
11 the results were similar to those obtained using the eSD model. In the case of strong
12 dipolar couplings a Thermal Mixing mechanism in the rotating frame could provide the
13 calculated EPR spectra under MW irradiation.(Abragam, 1961; de Boer, 1976;
14 Borghini, 1968; Goldman, 1970; Provotorov, 1962; Wenckebach, 2016; Wollan, 1976)
15 These studies also contributed to the validity of the iCE model in the weak and the
16 strong dipolar coupling regime.

17 In addition to the CE mechanism, leading to the main nuclear signal enhancements at
18 relatively high radical concentrations, the solid effect (SE) process also influences these
19 enhancements. This process contributes to the signal enhancements, but in addition
20 causes some electron depolarization that in turn can influence the CE enhancement
21 process(Hovav et al., 2015b; Leavesley et al., 2018). When nitroxide radicals are used
22 as DNP polarizers, these SE depolarization effects arise from ^1H and ^{14}N nuclei
23 hyperfine interactions(Kundu et al., 2018b; Leavesley et al., 2017). The SE induced
24 electron polarization depletions are highly evident in ELDOR spectra at concentrations
25 that are below the usual concentration used for DNP, but their influence is observed
26 also at concentrations around 20 mM, which are relevant for DNP(Harris et al., 2011;
27 Thankamony et al., 2017). As the Λ^{eSD} constants are determined from ELDOR
28 lineshapes, the SE effects should be taken into account in the eSD model to ensure the
29 extraction of their correct value. The purpose of this study is to account explicitly for
30 the effects of the SE mechanism on ELDOR lineshapes for nitroxides and to explore its
31 influence on the extraction of the Λ^{eSD} parameter at concentrations relevant for static
32 DNP.

1 We started this study by measuring ELDOR spectra of a 0.5 mM TEMPOL in DMSO
2 frozen solution, in which the SE is the sole mechanism of depolarization, as the spectral
3 diffusion mechanism is negligible. To analyze these ELDOR spectra we established a
4 theoretical framework that accounts for all ^{14}N -SE and ^1H -SE depletions observed in
5 these spectra. For this low concentration, the ELDOR spectrum is identical to the
6 ELDOR detected NMR (EDNMR) spectrum of nitroxide, which has already been
7 studied and simulated in the past(Cox et al., 2017; Florent et al., 2011; Jeschke and
8 Spiess, 1998; Kaminker et al., 2014; Nalepa et al., 2014, 2018). Yet, there is one major
9 difference: Under EDNMR conditions, where resolution is of prime interest, the MW
10 irradiation period is short, in the microsecond range, and therefore relaxation processes
11 play a limited role during that irradiation. However, under DNP conditions the duration
12 of the irradiation is in the range of milliseconds or longer and the electron and nuclear
13 relaxation processes influence the magnitude of the depolarization. A second, more
14 technical, difference is that in a full field-frequency two dimensional (2D) EDNMR
15 spectrum the EPR dimension is usually obtained by stepping the magnetic field(Florent
16 et al., 2011; Jeschke and Spiess, 1998; Kaminker et al., 2014; Nalepa et al., 2014, 2018)
17 unless chirped pulses are being used(Wili and Jeschke, 2018), while 2D ELDOR maps
18 in the context of DNP are obtained by stepping the frequency. In some earlier works
19 the contributions from different nuclei in the EDNMR spectra were taken into account
20 by superimposing their individual spectra ignoring the contributions of combination
21 frequencies(Tan et al., 2019; Wang et al., 2018). In others, the combinations were also
22 taken into account and reproduced in the simulated spectra (Cox et al., 2017). The
23 appearance of these lines depends on the experimental conditions (Cox et al., 2017).
24 As under DNP conditions the duration of the microwave irradiation is long we also took
25 into account for ^{14}N - ^1H combination lines in the ELDOR spectral simulations.

26 After analyzing the 0.5 mM spectrum, we proceeded to 10 and 20 mM TEMPOL
27 solutions, where spectral diffusion becomes significant. We measured their ELDOR
28 spectra and analyzed them employing the eSD model(Hovav et al., 2015b), taking into
29 account the SE mechanism through an ad-hoc inclusion of the ^{14}N and ^1H frequencies.

30 **2. Methods and Materials**

31

32 **2.1 Sample preparation**

1 Samples of 2-3 μl in 0.6 mm ID x 0.84 mm quartz tubes, with 0.5, 10 and 20 mM
 2 TEMPOL dissolved in a solution of DMSO/H₂O (1:1 v/v), were degassed by a *Freeze-*
 3 *Pump-Thaw* procedure and fast frozen with liquid nitrogen. TEMPOL and DMSO were
 4 both purchased from Sigma Aldrich and used as is.

5 2.2 Spectroscopic measurements

6 All measurements were carried out on our W-band (95 GHz, 3.4 T) homebuilt EPR
 7 spectrometer(Goldfarb et al., 2008; Mentink-Vigier et al., 2013) at 20 K.

8 Echo-detected EPR (ED-EPR) spectra were measured using the pulse sequence $\pi/2$ - τ -
 9 π - τ -echo with $\tau=600$ ns, while increasing the magnetic field stepwise from 3370 to
 10 3395 mT, with a 2 ms repetition time. The pulse lengths were 100 ns for the $\pi/2$ pulse
 11 and 200 ns for the π pulse, optimized at a detection frequency of 94.90 GHz.

12 Electron spin-lattice relaxation times T_{1e} were measured at different positions within
 13 the EPR spectrum by saturation recovery experiments with a long MW saturation pulse
 14 of 30 ms and echo pulses of 300 ns each as typical for DNP MW power. The T_{1e} curves
 15 were analyzed using a superposition of two exponential functions with time constants
 16 t_1 and t_2 , with the slow (and major) component assigned to T_{1e} .

17 The ELDOR pulse sequence is shown in Figure 1 and ELDOR spectra were measured
 18 at different detection frequencies along the EPR spectrum.. The spectrometer was set
 19 to low power as typical for DNP using the detection sequence α - τ - α - τ -echo, where α
 20 is a flip angle of less than $\pi/2$. While for EPR applications ELDOR is carried out at a
 21 fixed detection frequency and the magnetic field is varied to access different regions in
 22 the EPR spectrum, here we kept the field constant and varied the detection frequency
 23 to access the spectrum width as done for DNP applications. To carry out these ELDOR
 24 measurements, we increased the bandwidth of the cavity to accommodate the full

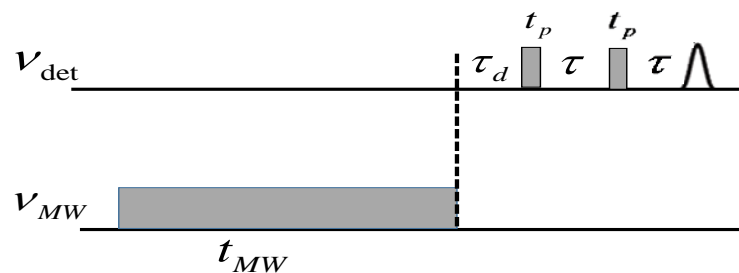


Figure 1. ELDOR pulse sequence, where v_{det} is the detection frequency , v_{MW} is the frequency of the pump pulse and t_{MW} is the duration of the pump pulse.

1 spectrum of TEMPOL (approx. 500 MHz). The cavity resonance was tuned to 94.80
 2 GHz. For the 0.5 mM sample ELDOR spectra (40 in total) were recorded as a function
 3 of the pump frequency, which was varied from 94.3 GHz to 95.3 GHz. To obtain 2D
 4 ELDOR data ELDOR spectra were measured at different detection frequencies in
 5 intervals of 10 MHz from 94.55 GHz to 94.95 GHz, which covers most of the EPR
 6 spectrum. The amplitude of the pump pulse, ν_1 , was 0.5 MHz, as determined by a
 7 nutation experiment at 94.8 GHz, corresponding to an inversion pulse of 1 μ s. The
 8 experimental parameters for the ELDOR experiments are listed in **Table 1**.

9
 10 **Table 1.** Parameters used in EDNMR experiment for 0.5, 10 and 20 mM radical concentration
 11 (see Fig. 1)

t_p	T	t_{MW}	Repetition time	τ_d
300 ns	600 ns	10 ms	20 ms	6 μ s

12 13 **3 Simulations**

14 **3.1 Low radical concentrations**

15 *The Hamiltonian and the allowed transition*

16 In an effort to analyze the ELDOR spectra of the 0.5 mM TEMPOL solution we rely on
 17 quantum mechanical based calculations considering the spin evolution of a three-spin
 18 system consisting of an electron spin, $S=1/2$, coupled to a single ^1H nucleus and a
 19 single ^{14}N nucleus. Simulations of these ELDOR spectra were performed using a
 20 modified version of the computer code developed by Kaminker *et al.* (Kaminker et al.,
 21 2014) for a two-spin system; one electron spin and one ^{14}N nucleus. The simulated
 22 ELDOR spectra comprise of EPR signals calculated at fixed detection frequency
 23 positions $\nu_{\text{det}} = \omega_{\text{det}} / 2\pi$ as a function of the of pump pulse frequency, $\nu_{MW} = \omega_{MW} / 2\pi$.

24 In these calculations, we had to take into account the fact that the duration of the MW
 25 irradiation in DNP experiments t_{MW} is much longer than commonly used in EDNMR
 26 spectroscopy (ms vs μ s range, respectively). For such long irradiation times the three-
 27 spin calculations cannot account for the experimental spectral observations, mainly due
 28 to the fact that the real spin system is more extended than only three spins because of
 29 the many coupled protons present in the sample. Accordingly, without extending the
 30 number of spins in our model we had to modify Kaminker's procedure to reproduce the
 31 experimental observations, as will be discussed here below.

1 The three-spin system is described by the following spin Hamiltonian in the MW
 2 rotating frame, assuming the high field approximation:

3

$$\begin{aligned}
 \hat{H}_{\theta,\varphi} = & \Delta\omega_e \hat{S}_z - \omega_N \hat{I}_{zN} - \omega_H \hat{I}_{zH} + A_{zz}^H \hat{S}_z \hat{I}_{zH} + A_{zz}^N \hat{S}_z \hat{I}_{zN} \\
 & + (A_H^+ \hat{I}_H^+ + A_H^- \hat{I}_H^-) \hat{S}_z + (A_N^+ \hat{I}_N^+ + A_N^- \hat{I}_N^-) \hat{S}_z + \hat{I}_N \cdot \tilde{Q} \cdot \hat{I}_N
 \end{aligned} \quad (1)$$

5 where

$$\Delta\omega_e \hat{S}_z = (\mu_B B_0 g_{eff}(\theta, \varphi) - \omega_{MW}) \hat{S}_z . \quad (2)$$

7 In Eq. 1 we neglected the dipolar interaction between the nuclei. $\Delta\omega_e$ is the off-
 8 resonance electron frequency, B_0 is the strength of the external magnetic field, pointing
 9 along the z-axis of the laboratory frame, and $g_{eff}(\theta, \varphi)$ is the effective g-tensor
 10 parameter for a specific orientation of the magnetic field with respect to the principle
 11 axis system of the g-tensor, given by the polar angles θ and φ . The g tensor used for
 12 the calculation is $g = [2.0065, 2.0037, 1.9997]$, obtained by simulating, using
 13 Easyspin(Stoll and Schweiger, 2006), the frequency domain EPR spectrum extracted
 14 from the echo intensity of the ELDOR spectra with the pump pulse set far outside the
 15 EPR spectrum (see Fig. S1 in ESI). The g-values obtained from the EPR simulations
 16 and further used in the EDNMR simulations differ from those reported by Florent et al
 17 (Florent et al., 2011) ($g = [2.00988, 2.00614, 2.00194]$) as they compensate for an error
 18 of 4 mT in the determination of B_0 . These g-values were used to determine the selected
 19 orientations and to calculate g_{eff} in Eq. 2. Because the energies and their differences
 20 depend on the product $g_{eff} B_0$, where the error in B_0 has been compensated in g, they
 21 are not affected by the error in the field. The shift of 4 mT in B_0 results in a shift of the
 22 proton frequency by 0.17 MHz, which is very small compared to the EDNMR
 23 linewidth. For ^{14}N it is even smaller and therefore the errors in the nuclei Larmor
 24 frequencies are negligible. The Larmor frequencies of ^1H and ^{14}N are $\omega_H = 2\pi\nu_H$ and
 25 $\omega_N = 2\pi\nu_N$, respectively. In the EPR high field approximation the terms that contribute
 26 to the hyperfine interaction are the secular and pseudo-secular terms with coefficients
 27 (A_{zz}^H, A_H^\pm) for ^1H and (A_{zz}^N, A_N^\pm) for ^{14}N , where $A_\pm^K = A_{zx}^K \pm iA_{zy}^K$, $K = \text{H, N}$. In the case of
 28 ^{14}N the hyperfine tensor contains an isotropic contribution $a_{iso}^N \neq 0$ in addition to the
 29 anisotropic tensor elements $[a_{zz}^K, a_{xx}^K, a_{yy}^K]$, where X, Y and Z are its principle axes.

1 Assuming that the two anisotropic hyperfine interactions are of axial symmetry (i.e.
2 $a_{XX}^K = a_{YY}^K = -1/2a_{ZZ}^K$) and that their major principal axes coincide with that of the g -
3 tensor, the hyperfine coefficients of $\hat{H}_{\theta,\varphi}$ become
4 $A_{zz}^K \equiv A_{zz}^K(\theta) = a_{iso}^K + \frac{1}{2}a_{ZZ}^K(3\cos^2\theta - 1)$ and $A_{\pm}^K \equiv A_{\pm}^K(\theta) = \frac{3}{2}a_{ZZ}^K \cos\theta \sin\theta$ (Schweiger
5 and Jeschke, 2001). In the case of TEMPOL, the isotropic ^{14}N contribution is
6 $a_{iso}^N = 44$ MHz and the anisotropic value is $-a_{ZZ}^N = 55$ MHz. The ^1H hyperfine value
7 was taken as $a_{ZZ}^H = 3$ MHz. Finally, the ^{14}N nuclear quadrupole interaction is also
8 included in the spin Hamiltonian. Here we used the principal values of the quadrupole
9 tensor obtained by Florent *et al.* (Florent *et al.*, 2011),
10 $(Q_{XX}, Q_{YY}, Q_{ZZ}) = (0.48, 1.29, -1.77)$ MHz, and again assumed that its principal axes
11 coincides with those of the g - tensor.

12 The MW irradiation Hamiltonian in the rotating frame is defined as

$$13 \quad \hat{H}_{MW} = \omega_1 \hat{S}_x . \quad (3)$$

14 At the start of all our simulations, the Hamiltonian for each set of (θ, φ) angles is
15 represented in matrix form, in the twelve product states of the basis sets in the laboratory
16 frame $|\chi_e\rangle, |\chi_H\rangle$ with $\chi_{e,H} = \alpha, \beta$ and $|\chi_N\rangle$ with $\chi_N = +1, 0, -1$, and diagonalized
17 according to

$$18 \quad \hat{\Lambda}_{\theta,\varphi} = \hat{D}_{\theta,\varphi}^{-1} \hat{H}_{\theta,\varphi} \hat{D}_{\theta,\varphi} . \quad (4)$$

19 $\hat{D}_{\theta,\varphi}$ is the diagonalization matrix and $\hat{\Lambda}_{\theta,\varphi}$ is the diagonal matrix consisting of the
20 eigenvalues $E_i^{\theta,\varphi}$, in frequency units, corresponding to the 12 eigenstates $|\lambda_i^{\theta,\varphi}\rangle$ with
21 $i = 1, \dots, 12$. The EPR transition probabilities between levels $|\lambda_i^{\theta,\varphi}\rangle$ and $|\lambda_j^{\theta,\varphi}\rangle$ are :

$$22 \quad P_{i,j}^{\theta,\varphi} = 2 \left| \langle \lambda_i^{\theta,\varphi} | D_{\theta,\varphi}^{-1} \hat{S}_x D_{\theta,\varphi} | \lambda_j^{\theta,\varphi} \rangle \right|^2 . \quad (5)$$

23
24 When $|Q_{ZZ}| < \omega_N < \frac{1}{2}a_{ZZ}^N, a_{iso}^N$, the $\omega_N I_{z,N}$ term in all Hamiltonians $\hat{H}_{\theta,\varphi}$ has little influence
25 on the form of the eigenstates, which are products of the electron states $|\chi_e\rangle$ with the
26 eigenvalues $m_e = \pm 1/2$, the hyperfine mixed proton states approximately equivalent to $|\chi_H\rangle$

1 with $m_H \approx \pm 1/2$ and the nitrogen states $|\chi_N\rangle$, mainly determined by the hyperfine interaction
 2 terms in $\hat{H}_{\theta,\varphi}$ with $m_N \approx +1, 0, -1$. As a result we can easily recognize six “allowed”
 3 transition with frequencies $\nu_{(i,j)_a}(\theta, \varphi) = (E_i^{\theta,\varphi} - E_j^{\theta,\varphi})$ that correspond to EPR transitions
 4 $(i - j)_a$, with $\Delta m_e = \pm 1$, $\Delta m_H \approx 0$ and $\Delta m_N \approx 0$ and thus $P_{i,j}^{\theta,\varphi} \approx 1$. We note that for
 5 orientations along the X,Y axis, the ^{14}N hyperfine interaction is close to ω_N and therefore
 6 $P_{i,j}^{\theta,\varphi} < 1$. Figure 2 presents a schematic energy level diagram of the three-spin system
 7 for an arbitrary set of angles (θ, φ) . The six allowed transitions are indicated by red
 8 arrows. For one of these transitions the corresponding homonuclear “single quantum”

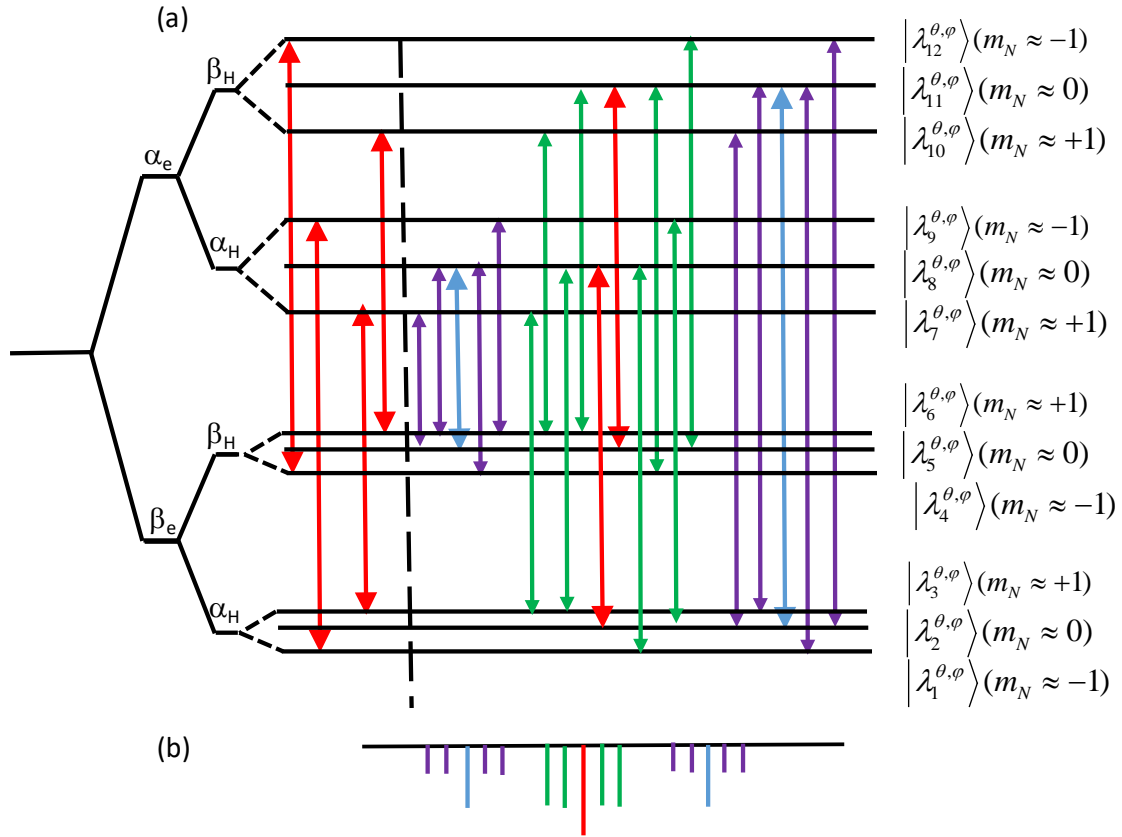


Figure 2. (a) A schematic energy level diagram of the three spin system with angles (θ, φ) , corresponding to an allowed transition. The eigenstates $|\lambda_i^{(\theta,\varphi)}\rangle$ are characterized by their m_N values and product states of $|\chi_e\rangle$, $|\chi_H\rangle$ and $|\chi_N\rangle$. The energy level differences ν_e and $\nu_H \pm A_H$ are scaled arbitrarily. On the left of the energy level diagram the allowed transitions (3-7), (6-10), (1-9), (4-12) are indicated by the red arrows. On the right the red arrows correspond to the allowed transition between the states with sub-indexes (2-8) and (5-11). The nitrogen forbidden transitions (2-9), (2-7), (4-11) and (6-11) are assigned by the green arrow and the proton forbidden transitions (2-11) and (5-8) by the blue arrows. The purple arrows indicate the combined proton-nitrogen transitions. (b) A schematic presentation of the ELDOR spectrum corresponding to overlapping allowed (2-8) and (5-11) transitions following the color coding of the arrows.

1 (SQ) forbidden transitions, with $\Delta m_H \approx \pm 1$ or $\Delta m_N \approx \pm 1$, are also indicated, in blue or
 2 green, respectively. The heteronuclear “double-” and “zero quantum” (DQ and ZQ)
 3 forbidden transitions, with $\Delta m_H \approx \pm 1$ and $\Delta m_N \approx \pm 1$, are shown in purple.

4 Using the Orisel function in Easyspin(Stoll and Schweiger, 2006), the values of $E_i^{\theta,\varphi}$
 5 and $P_{i,j}^{\theta,\varphi}$ were calculated for a collection of 9609 sets of values of (θ, φ) and from them
 6 all transition frequencies $\nu_{i,j}(\theta, \varphi)$ were determined. To choose which orientations of
 7 the spin system contribute to the allowed EPR signal at a given ν_{det} , we search for those
 8 sets of angles (θ, φ) for which at least one allowed transition falls in the frequency
 9 range $\nu_{\text{det}} - 3\text{MHz} \leq \nu_{(i,j)_a}(\theta, \varphi) \leq \nu_{\text{det}} + 3\text{MHz}$. This frequency span provides a
 10 frequency bandwidth of 6 MHz for the detection pulse, estimated as the excitation
 11 bandwidth for a detection pulse of 300 ns length. In addition, it can account for some
 12 g- and hyperfine strain. This procedure generated a subset of selected $(\theta, \varphi)_{\text{det}}$ pairs for
 13 each ν_{det} , the size of which depends on the position of ν_{det} within the EPR spectrum.

14 After choosing a value for ν_{det} we simulated the ELDOR spectra of all crystal
 15 orientations of the subset $(\theta, \varphi)_{\text{det}}$. The sum of these spectra are compared with the
 16 measured ELDOR spectrum at that frequency. To obtain the individual ELDOR spectra
 17 we calculated the EPR signal at ν_{det} after a long MW pump pulse as a function of the
 18 frequency of this pulse, ν_{MW} .

19 *The population rate equation*

20 To follow the evolution of the spin system during the long MW irradiation period, prior
 21 to the EPR detection, it is sufficient to consider only the eigenstate populations $p_i^{\theta,\varphi}(t)$
 22 of all $|\lambda_i^{\theta,\varphi}\rangle$ for the detection subset, as described earlier (Hovav et al., 2010, 2015b).

23 The rate equation during the MW irradiation for these populations can be presented as

$$24 \quad \frac{d}{dt} p_i^{\theta,\varphi} = \sum_{j=1,12} \{-R_{ij}^{\theta,\varphi} + W_{ij}^{\theta,\varphi}\} p_j^{\theta,\varphi}, \quad (6)$$

25 where $R_{ij}^{\theta,\varphi}$ are the elements of the 12x12 spin lattice relaxation matrix $\hat{R}_{\theta,\varphi}$ and $W_{ij}^{\theta,\varphi}$ are the
 26 elements of the 12x12 MW rate matrix $\hat{W}_{\theta,\varphi}$. The relaxation matrix $\hat{R}_{\theta,\varphi}$ is equal to the sum of
 27 the relaxation matrices $\hat{r}_{(ij)}^{\theta,\varphi}$ of all transitions $\{i-j\}$ with $E_j > E_i$. The non-zero matrix
 28 elements of $\hat{r}_{(ij)}^{\theta,\varphi}$ are derived, assuming a linear field fluctuation causing T_{1e} :

$$r_{(ij),ii}^{\theta,\varphi} = -\frac{1}{T_{1,ij}} \frac{1}{(1+\eta_{ij})} ; \quad r_{(ij),ij}^{\theta,\varphi} = \frac{1}{T_{1,ij}} \frac{\eta_{ij}}{(1+\eta_{ij})}, \quad (7a)$$

$$r_{(ij),ji}^{\theta,\varphi} = \frac{1}{T_{1,ij}} \frac{1}{(1+\eta_{ij})} ; \quad r_{(ij),jj}^{\theta,\varphi} = -\frac{1}{T_{1,ij}} \frac{\eta_{ij}}{(1+\eta_{ij})}$$

and

$$\frac{1}{T_{1,ij}} = \frac{\left| \langle \lambda_i^{\theta,\varphi} | \hat{S}_x | \lambda_j^{\theta,\varphi} \rangle \right|^2}{T_e} \quad (7b)$$

with $\eta_{ij}^{\theta,\varphi} = p_i^{\theta,\varphi;eq} / p_j^{\theta,\varphi;eq}$ being the ratio between the thermal equilibrium populations defined in the laboratory frame, and

$$\hat{R}_{\theta,\varphi} = \sum_{\{i-j\}} \hat{r}_{(ij)}^{\theta,\varphi}. \quad (7c)$$

The elements of $\hat{W}_{\theta,\varphi}$ are equal to the sum of the $\hat{w}_{(ij)}^{\theta,\varphi}$ matrices with non-zero elements that express the effective irradiation strength on each transition $(i-j)$ (Hovav et al., 2010):

$$w_{(ij),ij}^{\theta,\varphi} = w_{(ij),ji}^{\theta,\varphi} = -w_{(ij),ii}^{\theta,\varphi} = -w_{(ij),jj}^{\theta,\varphi} = \frac{\omega_1^2 \left| \langle \lambda_i^{\theta,\varphi} | \hat{S}_x | \lambda_j^{\theta,\varphi} \rangle \right|^2 T_{2mw}}{1 + 4\pi^2 \left\{ \nu_{ij}^{\theta,\varphi} - \nu_{MW} \right\}^2 T_{2mw}^2} \quad (8a)$$

and

$$\hat{W}_{ij}^{\theta,\varphi} = \sum_{(i-j)} \hat{w}_{(ij)}^{\theta,\varphi}. \quad (8b)$$

Here ω_1 is the MW amplitude (see Eq. 3). A transverse relaxation time T_{2mw} , which determines the off-resonance efficiency of the irradiation, is introduced and for simplicity is assumed to be the same for all transitions. Note that T_{2mw} is not the measured phase memory time, T_M . After entering the values of T_{1e} , ω_1 and an irradiation time, it is possible to solve Eq. 6 and to use the populations at the end of the irradiation to evaluate the EPR signals.

Setting the detection frequency at one of the allowed transition frequencies and irradiating with a pump frequency that matches one of its associated forbidden transitions (i.e, they share a common energy level) result in a depletion of the EPR signal. The calculations show that the depletion can be very significant for pump pulses on the order of tens of microseconds but disappears for irradiation periods of the order

1 of tens of milliseconds. Thus using Eq. 6 works well for calculating EDNMR spectra
 2 for short pump pulses(Kaminker et al., 2014; Ramirez Cohen et al., 2017). However,
 3 for extended periods of MW irradiation, longer than T_{1e} as is applied in DNP, the
 4 simulated ELDOR signals are very weak at the forbidden transition frequencies. The
 5 reason for this is that for MW irradiations longer than T_{1e} , the SE spin evolution of an
 6 electron-nuclear spin pair brings the electronic polarization back to its equilibrium
 7 value. This is, however, in contrast to the experimental results where rather intense lines
 8 were observed even for long irradiation. The reason for this discrepancy is that in reality
 9 the electron spins are interacting with several equivalent coupled nuclei, which transfer
 10 their polarization to the bulk via nuclear spin diffusion. This is particularly true when
 11 many protons are present. Accordingly, to reproduce the experimental results, while
 12 still employing our simplified three-spin system model, requires modification of the
 13 simulation procedure as described next.

14 *Modification of the rate equation*

15 In order to obtain from a three-spin calculation the observed EPR signal depletions even
 16 after long irradiation periods, we modified the form of the MW rate matrix. Realizing
 17 that an irradiation of one of the forbidden transitions, $(i-k)_f$ and $(k-j)_f$, causes a
 18 depletion of the population difference of an allowed transition, $(i-j)_a$, we removed
 19 the four matrix elements of $\hat{W}_{(ik)_f}^{\theta,\varphi}$ and $\hat{W}_{(kj)_f}^{\theta,\varphi}$ from the $\hat{W}_{\theta,\varphi}$ matrix. This is equivalent
 20 to removing the irradiation on the forbidden transitions, which in turn cause the change
 21 in population difference of the allowed transition, $P_{i,j}^{\theta,\varphi}$. To re-introduce the effect of
 22 the forbidden transitions on $P_{i,j}^{\theta,\varphi}$ of the allowed transitions, we added them as an
 23 artificial irradiation on the allowed one by adding them to the four non-zero matrix
 24 elements of $\hat{W}_{(ij)_a}^{\theta,\varphi} : \left\{ \hat{W}_{(ik)_f}^{\theta,\varphi} + \hat{W}_{(kj)_f}^{\theta,\varphi} \right\}_{(ij)_a}$. In this way we ensure a depletion of the
 25 population difference of $(i-j)_a$, without the relaxation mechanism cancelling it.
 26 Realizing that the depletion during the simulations is now dependent on the value of
 27 $T_{i,j}$, we introduce SE fitting parameters to adjust their values during irradiation: one
 28 for each of the different forbidden proton, a_H^{SE} , nitrogen, a_N^{SE} , combined proton-
 29 nitrogen, a_{HN}^{SE} and even double quantum (DQ) nitrogen, a_{DQ-N}^{SE} transitions. In this way

1 an irradiation on $(i-k)_f$ reproduced the experimentally observed signal depletions,
 2 still taking into account the effective MW irradiation strengths, $\omega_1 \times \langle \lambda_i^{\theta,\varphi} | \hat{S}_x | \lambda_k^{\theta,\varphi} \rangle$,
 3 and its original off resonance efficiency. Performing this procedure for all forbidden
 4 transitions, the modified $\hat{W}_{\theta,\varphi}$ matrix contains only elements corresponding to the
 5 allowed transitions $(i-j)_a$:

$$\begin{aligned}
 \hat{W}_{\theta,\varphi} &= \sum_{\substack{6 \text{ allowed} \\ (i-j)_a}} \hat{W}_{(ij)_a}^{\theta,\varphi} ; \\
 \hat{W}_{(ij)_a}^{\theta,\varphi} &= \hat{w}_{ij}^{\theta,\varphi} + a_N^{SE} \sum_{(ik)_N:(kj)_N} \left\{ \hat{w}_{(ik)_N}^{\theta,\varphi} + \hat{w}_{(kj)_N}^{\theta,\varphi} \right\}_{(ij)_a} + a_{DQ-N}^{SE} \sum_{(ik)_{DQ-N}:(kj)_{DQ-N}} \left\{ \hat{w}_{(ik)_{DQ-N}}^{\theta,\varphi} + \hat{w}_{(kj)_{DQ-N}}^{\theta,\varphi} \right\}_{(ij)_a} \\
 &\quad + a_H^{SE} \sum_{(ik)_H:(kj)_H} \left\{ \hat{w}_{(ik)_H}^{\theta,\varphi} + \hat{w}_{(kj)_H}^{\theta,\varphi} \right\}_{(ij)_a} + a_{HN}^{SE} \sum_{(kl)_{HN}:(lk)_{HN}} \left\{ \hat{w}_{(kl)_{HN}}^{\theta,\varphi} + \hat{w}_{(lk)_{HN}}^{\theta,\varphi} \right\}_{(ij)_a}
 \end{aligned} \tag{9}$$

6
 7
 8
 9 Here the sums over k and l of $(ik)_K$, $(kj)_K$, $(kl)_{KK'}$, $(lk)_{KK'}$ are restricted to the homo-
 10 nuclear and hetero-nuclear forbidden transitions only. After this modification it
 11 becomes possible to write for each allowed transition $(i-j)_a$ a 2x2 rate equation for
 12 the populations $p_i^{\theta,\varphi}(i)$ and $p_j^{\theta,\varphi}(t)$ with a rate matrix $(-\hat{r}_{(ij)_a} + \hat{W}_{(ij)_a}^{\theta,\varphi})$.

13 The actual relaxation pathways in the spin system is influenced by all the elements of
 14 $\hat{R}_{\theta,\varphi}$ and as a result, an irradiation on one allowed transition can have a small effect on
 15 the populations of another allowed transition. (Kaminker et al., 2014) Our modification
 16 caused this effect to vanish in the simulations. To reintroduce it we added to each
 17 $\hat{W}_{(ij)_a}^{\theta,\varphi}$ the MW rate matrices of the other transitions $\hat{W}_{(kl)_a}^{\theta,\varphi}$, while introducing an
 18 additional small fitting parameter a_{a-a} :

$$\hat{W}_{(ij)_a}^{\theta,\varphi} = \hat{W}_{(ij)_a}^{\theta,\varphi} + a_{a-a} \sum_{\substack{(kl)_a \\ k,l \neq i,j}} \left\{ \hat{W}_{(kl)_a}^{\theta,\varphi} \right\}_{(ij)_a} \tag{10}$$

19
 20 Choosing values for all fitting parameters and inserting values for T_{1e} and T_{2mw} , the
 21 populations of the allowed transitions corresponding to $(\theta,\varphi)_{\text{det}}$ at the end of a MW
 22 pump period t_{MW} at frequency ν_{MW} can now be obtained using Eq. 10. The EPR signal
 23 $E_{\text{det}}(\nu_{\text{det}}, t_{MW})$ at ν_{det} can then be calculated by taking the Hamiltonian diagonalization
 24 into account and by solving Eq. 6 with the modified MW rate matrices for each set of

1 angles (φ, θ) . Adding all $(p_{i_a}^{\theta, \varphi} - p_{j_a}^{\theta, \varphi})(t_{MW})$ values belonging to $(\theta, \varphi)_{\text{det}}$ and
 2 normalizing their sum $S_{\text{det}}(\nu_{MW}, t_{MW})$ to the sum $S_{\text{det}}^{\text{ref}}(t_{MW})$ of all $(p_{i_a}^{\theta, \varphi} - p_{j_a}^{\theta, \varphi})(t_{MW})$
 3 belonging to $(\theta, \varphi)_{\text{det}}$, obtained by again solving Eq. (10) but this time for a ν_{MW} value
 4 far removed from the frequency range of all allowed and forbidden transitions:

$$5 \quad E_{\text{det}}(\nu_{MW}, t_{MW}) = S_{\text{det}}(\nu_{MW}, t_{MW}) / S_{\text{det}}^{\text{ref}}(t_{MW}) \quad (11).$$

6 Plotting $E_{\text{det}}(\nu_{MW}, t_{MW})$ as a function of ν_{MW} , and after line smoothing over 5 MHz,
 7 results in a ELDOR spectrum at ν_{det} . (see Fig. 2).

8 **3.2 High radical concentrations**

9 To simulate the ELDOR spectra of the 10 mM and 20 mM samples we used the eSD
 10 model (Hovav et al., 2015b). This computational model divides the EPR spectrum into
 11 frequency bins and calculates the electron polarizations $P_b(t_{MW})$ of each bin at
 12 frequency ν_b . It consists of a set of coupled rate equations for these polarizations with
 13 rate constants describing the effects of spin lattice relaxation, eSD polarization
 14 exchange and MW irradiation. To take the SE into account the MW rate constants of
 15 each $P_b(t_{MW})$, are extended by effective SE terms (Hovav et al., 2015b; Kundu et al.,
 16 2018b; Wang et al., 2018):

$$17 \quad w_{MW}^b = \frac{\omega_1^2 T_{2mw}}{1 + 4\pi^2 (\nu_b - \nu_{MW})^2 T_{2mw}^2} + \sum_{K=H, N, H-N} \frac{(A_K^{SE} \omega_1)^2 T_{2mw}}{1 + 4\pi^2 (\nu_b \pm \nu_K - \nu_{MW})^2 T_{2mw}^2}. \quad (12)$$

18 Here ν_K are the ^1H and ^{14}N nuclear frequencies and A_H^{SE} , A_N^{SE} and A_{H-N}^{SE} are fitting
 19 parameters used to scale the MW power on the forbidden transition and they just affect
 20 the SE peak intensities of the ELDOR peaks and not their positions. The eSD exchange
 21 rate constants between the polarizations in bin b and bin b' are defined by the exchange
 22 rate coefficients

$$23 \quad r_{b,b'}^{eSD} = \frac{\Lambda^{eSD}}{4\pi^2 (\nu_b - \nu_{b'})^2}, \quad (13)$$

24 where the parameter Λ^{eSD} determines the time scale of the spectral diffusion process.
 25 After solving the polarization rate equations for an irradiation frequency ν_{MW} the

1 polarization $P_{\text{det}}(\nu_{MW})$ at the detection frequency ν_{det} is obtained and divided by its
 2 Boltzman equilibrium value $P_{\text{det}}^{\text{eq}}$ to obtain the ELDOR signal

$$3 \quad E(\nu_{MW}, \nu_{\text{det}}, t_{MW}) = \frac{P_{\text{det}}(\nu_{MW})}{P_{\text{det}}^{\text{eq}}} \quad (14).$$

4

5 **4 Results and Discussion**

6 **4.1 ELDOR spectra of the 0.5 mM TEMPOL**

7 Experimental ELDOR spectra of the 0.5 mM TEMPOL were obtained by recording
 8 EPR echo intensities as a function of ν_{MW} for fixed ν_{det} and t_{MW} values, using the
 9 experimental parameters summarized in the Experimental section. The results
 10 $E(\nu_{MW}; \nu_{\text{det}}, t_{MW})$ were analyzed using the procedure described in the Simulation
 11 section. From the many ELDOR spectra measured in this way, we show in Fig. 3 (black
 12 traces) only three, each one with a different detection frequency ν_{det} within the EPR
 13 spectrum. The dips in the ELDOR spectra, also referred to as EDNMR spectra, appear
 14 at the frequencies of the allowed and forbidden transitions, dictated by the ^1H and ^{14}N
 15 Larmor frequencies ν_H and ν_N and their hyperfine interactions (A_{zz}^H, A_H^\pm) for ^1H and
 16 (A_{zz}^N, A_N^\pm) along with the quadrupole interaction for ^{14}N (Aliabadi et al., 2015; Cox et
 17 al., 2013, 2017; Kaminker et al., 2014; Nalepa et al., 2014; Ramirez Cohen et al., 2017;
 18 Rapatskiy et al., 2012). At W-band frequencies (~ 95 GHz) the ^1H frequencies are
 19 around 144 MHz and the ^{14}N frequencies are in the range $\sim 20 - 70$ MHz, as reported
 20 earlier in EDNMR experiments (Florent et al., 2011; Kaminker et al., 2014; Nalepa et
 21 al., 2014; Wili and Jeschke, 2018). Thus we expect in addition to the homo-nuclear
 22 forbidden transition signals additional signals around -144, 0 and +144 MHz each with
 23 a possible spread of -70 - +70 MHz, due to the hetero-nuclear forbidden transitions.

24 Fig. 3b shows the ELDOR spectrum for $\nu_{\text{det}} = 94.55$ GHz, where . This frequency falls
 25 in the g_z region of the EPR spectrum (Fig. 3a), which is characterized by its “single
 26 crystal like” features. As a result the ^{14}N signals are only slightly powder broadened
 27 and well resolved. (Florent et al., 2011; Kaminker et al., 2014) At this detection

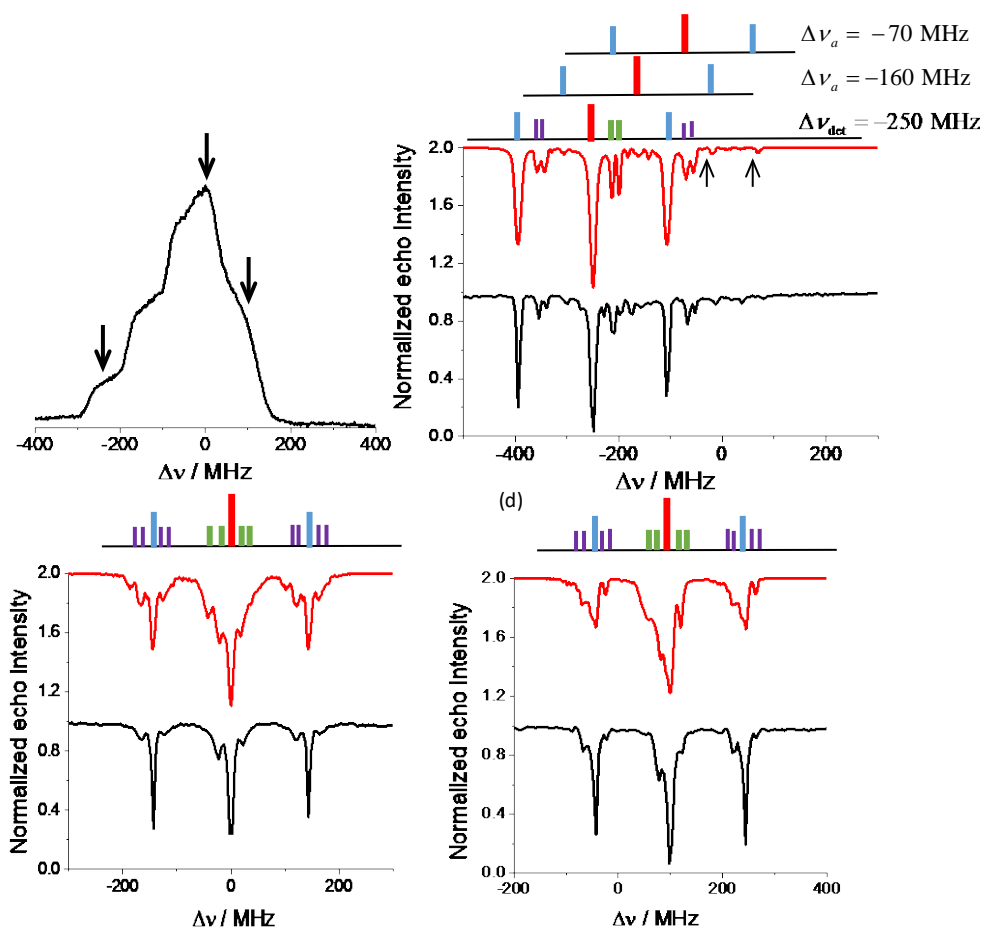


Fig. 3. (d) The EPR spectrum and the positions at which the ELDOR spectra shown in (b)-(d) were recorded. (b)-(d) Experimental (black) and simulated (red) ELDOR spectra along with the associated stick spectrum using the color codes shown in Fig. 2, with detection frequencies $\nu_{\text{det}} = 94.55, 94.8, 94.9$ GHz, for (b), (c), and (d) respectively. The frequency axis is plotted relative to the center of the EPR spectrum at 94.8 GHz such that $\Delta\nu = \nu_{\text{MW}} - 94800$. The (b) spectrum is the most resolved, it shows the ^{14}N DQ transitions as well as peaks due to the other four allowed transitions and their associated ^1H forbidden transitions (indicated by arrows) arising from off-resonance and relaxation effects. A schematic for the different transitions in this case are described by the stick diagram with $\Delta\nu_a$ the positions of the two pairs of allowed transitions. Experiments were performed at 20K.

- 1 frequency the contributions to the echo signal originate only from the two low
- 2 frequency allowed transitions (red in the $\Delta\nu_{\text{det}} = -250$ MHz stick diagram), split by the
- 3 ^1H hyperfine interaction, of the crystallites belonging to the “single crystal”. The MW
- 4 excitation is not selective enough to resolve the protons splitting. In Table S1 in the SI

1 the frequency assignments of the lines in the ELDOR spectra are correlated to the
 2 $(i-j)_a$ and $(i-j)_f$ transitions in Fig. 2, together with the color coding in the stick
 3 spectrum shown in Fig. 3b. The assignments of the other four allowed transitions are
 4 also tabulated, together with their ^1H - and ^{14}N -homonuclear forbidden transitions and
 5 the ^1H - ^{14}N -heteronuclear forbidden transitions. In the ELDOR spectra the two ^1H -
 6 transitions (in blue) and the four ^{14}N -transitions (in green) are clearly present. The ^1H -
 7 ^{14}N -transitions (in purple) are also detected. The additional spectral features must
 8 originate from the four non-directly detected allowed transitions with their forbidden
 9 transitions. Stick spectra of these allowed transitions and their ^1H -forbidden transitions
 10 are also added in Fig. 3b, and it is interesting to see that part of these lines in these
 11 spectra appear in the experimental ELDOR spectrum (marked by arrows in Fig. 3b).
 12 The appearance of signals corresponding to the non-directly excited allowed transition
 13 has been reported earlier (Kaminker et al., 2014) and was attributed to the combination
 14 of off-resonance and relaxation effects. In Fig. 3c the experimental ELDOR spectrum
 15 at $\nu_{\text{det}} = 94.8 \text{ GHz}$ (g_y) is plotted and a schematic stick spectrum is added on the top. All
 16 possible allowed transitions contribute to this spectrum and the spectral features are
 17 broadened and even hard to distinguish. The stick spectrum represents only one typical
 18 contribution to the observed powder spectrum. The same is true for the spectrum in Fig.
 19 3d at $\nu_{\text{det}} = 94.9 \text{ GHz}$ (g_x).

20 To simulate the experimental ELDOR spectra we needed to measure the T_{1e} values.
 21 These were measured at several frequency positions within the EPR spectrum: 20.8ms
 22 at $\nu_{\text{det}} = 94.6 \text{ GHz}$, 13.8 ms at $\nu_{\text{det}} = 94.8 \text{ GHz}$ and 15.8 ms at $\nu_{\text{det}} = 94.9 \text{ GHz}$, which vary
 23 with the position within the EPR spectrum, with the highest value obtained for the g_z
 24 region. In the simulations we used the average value of $T_{1e} = 16.7 \text{ ms}$.

25 The best fit simulated spectra that resemble the three experimental ELDOR spectra in
 26 Fig. 3 are shown in red. To achieve these spectra we used the following parameters:
 27 $T_{2mw} = 100 \mu\text{s}$, $t_{MW} = 100 \text{ ms}$ and the SE fitting parameters $a_H^{SE} = 10^3$, $a_N^{SE} = 0.5$,
 28 $a_{H-N}^{SE} = 10^3$ and $a_{a-a}^{SE} = 0.5 \times 10^{-3}$. These parameters were determined via manual fitting
 29 of the intensities of the different lines in the spectrum in Fig. 3b. The same parameters
 30 were used for the simulated spectra in Fig. 3c and 3d. The fact that the SE parameter of
 31 the ^1H -forbidden transitions is large, seems to be connected with the many protons

1 involved in the SE process in the sample. In addition to the above mentioned forbidden
 2 transitions, we added also ^{14}N double quantum effect in the simulations by introducing
 3 a SE parameter of $a_{DQ-N}^{SE} = 5$. Comparing the simulated and experimental spectra we
 4 observe all expected forbidden transitions and some lines originating from the non-
 5 observed allowed transitions and their forbidden transitions. The double quantum lines
 6 expected around $\Delta\nu = 200$ MHz are not clearly resolved. The calculated spectra in Fig.
 7 3c and 3d resemble the experimental spectra, although the relative intensities of the
 8 lines do not agree so well.

9 A contour plot of the experimental 2D-ELDOR spectrum of the 0.5 mM sample is
 10 shown in Fig. 4a. The positions of the lines corresponding to the allowed transitions
 11 appear at the intense central diagonal of the spectrum. The signals associated with the
 12 $\{\text{e}^{-14}\text{N}\}$ forbidden transitions are close to the central diagonal and clearly reveal the
 13 anisotropic character of the hyperfine interaction. Namely, the strongest shifts of the
 14 line positions, with respect to the allowed line positions, are about 40 MHz in the g_z
 15 region of the EPR spectrum and reduce to 20 MHz in the $g_{x,y}$ regime. The signals
 16 associated with the $\{\text{e}^{-1}\text{H}\}$ forbidden transitions are the intense lines parallel to the

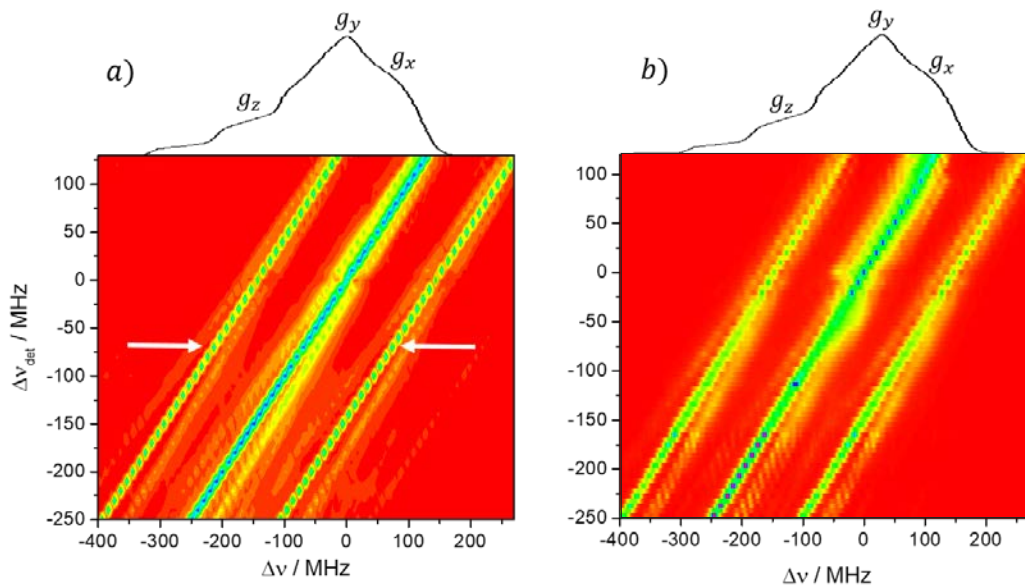
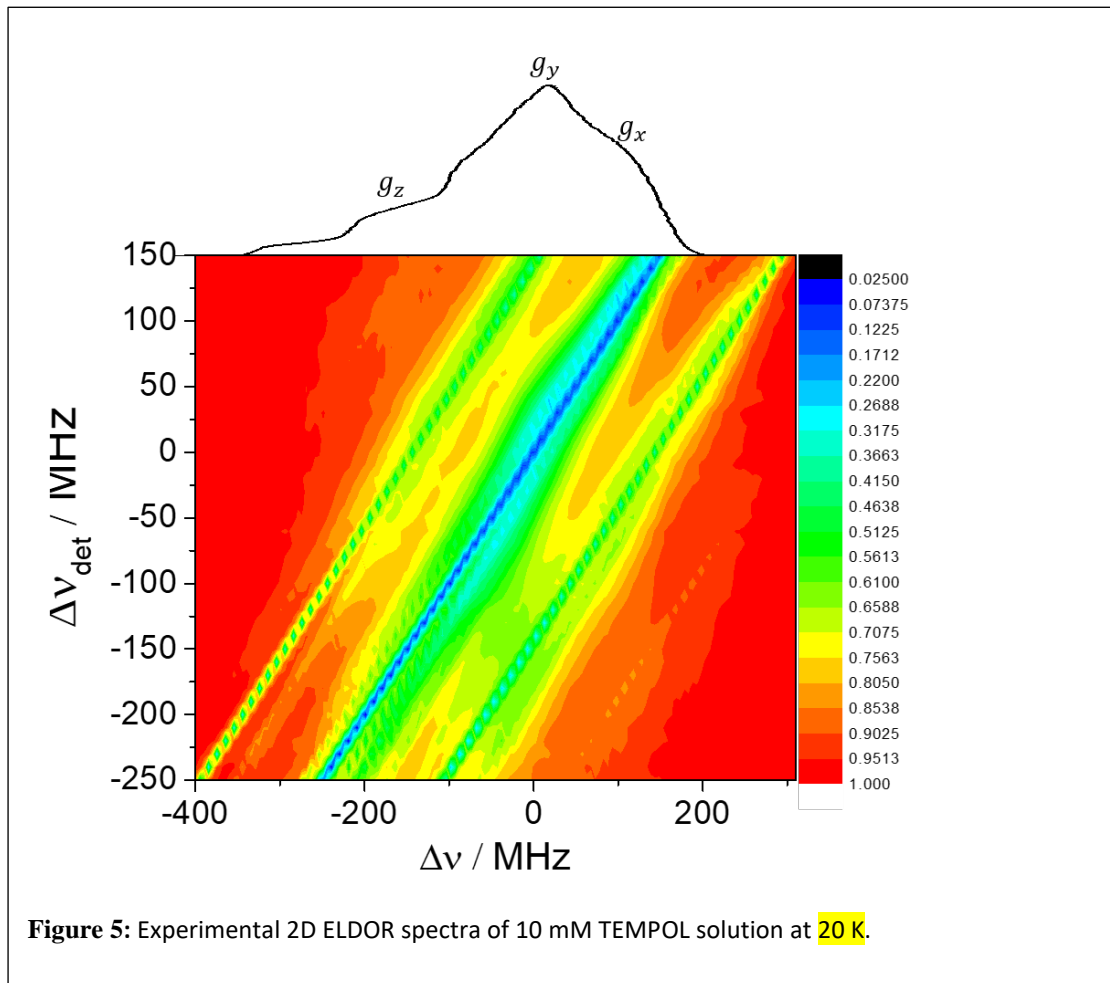


Figure 4. 2D contour ELDOR spectra of the 0.5mM sample (a) Experimental (20 K) and (b) simulated spectra where the y-axis is the off-resonance detection frequency ($\Delta\nu_{det} = \nu_{det} - 94.8$ GHz) and the x-axis is the off-resonance pump frequency ($\Delta\nu$). The central diagonal line corresponds to the allowed EPR transitions while the intense parallel lines on both its sides correspond to ^1H signals as indicated by white arrows in the experimental spectrum. The weaker lines around the center diagonal correspond to forbidden transitions involving ^{14}N and those about the outer ^1H lines are due to those involving both ^1H and ^{14}N

1 diagonal, and are surrounded by the signals coming from the $\{e^{-1}H^{-14}N\}$ forbidden
 2 transitions. Figure 4b shows the simulated 2D-ELDOR contour plot, which reproduces
 3 most of the features observed in the experimental contours. Some discrepancies can be
 4 observed in the intensities of the forbidden transition lines which can be attributed to
 5 the simplifications of the model.

6 4.2 ELDOR spectra of 10 mM and 20 TEMPOL

7 The 2D ELDOR spectrum for a 10 mM TEMPOL solution, presented in Fig. 5, displays
 8 the main features of the 1H SE solid effect lines, which run parallel to the diagonal. ^{14}N
 9 and combination lines are detectable but they are not as nicely resolved as in the 0.5
 10 mM sample. In addition, broad features that correspond to the depolarization of the
 11 electron spins owing to the eSD process are evident. To consider both SE and eSD
 12 effects we simulated the ELDOR spectra using the eSD model, including the influence
 13 of ^{14}N and 1H SE by incorporating the SE features as described in the Simulation section
 14 Eq. 12. We also measured T_{1e} along the EPR spectrum and the results are given in
 15 Fig. 6. T_{1e} displays an anisotropic behavior, namely it depends on the position within



1 the EPR spectrum with the largest variations observed in the g_z region (similar to our
 2 earlier observation for the 0.5 mM solution). Similar T_{1e} variations was also reported
 3 by Weber *et al*(Weber et al., 2017). To include the experimental T_{1e} values into the
 4 simulations, we assigned to each group of 5 consecutive bins, each one with a width
 5 of 2 MHz, the value of T_{1e} measured at the position in the EPR spectrum that
 6 correspond to those bins. Example of experimental and simulated ELDOR spectra for
 7 three positions of the detection frequency in the EPR spectrum are shown in Figure 7.

8 Initially the spectra were simulated using the eSD model considering only the ^1H SE
 9 effect (blue traces in Fig. 7), and the best fit gave an eSD parameter of $\Lambda^{eSD} = 60 \mu\text{s}^{-3}$.
 10 A better fit was obtained when taking into account ^{14}N SE, including the ^{14}N - ^1H
 11 combinations (green traces). This addition broadened the ELDOR lines resulting in a
 12 better match with the experimental result, with the same Λ^{eSD} value. Nevertheless,
 13 when ν_{det} reached the g_z region of the EPR spectrum (Fig. 7a, $\Delta\nu_{\text{det}} = -100$ MHz),
 14 the fit was not as good as in g_x (Fig. 7b, $\Delta\nu_{\text{det}} = 0$ MHz) and g_y (Fig. 7c, $\Delta\nu_{\text{det}} =$
 15 100 MHz). This implies that Λ^{eSD} might be anisotropic, which is unexpected. At this
 16 point we attribute this “apparent” anisotropy to the over simplified ad-hoc inclusion of
 17 the SE mechanism into the eSD model which does not fully account for the anisotropy
 18 of the ^{14}N hyperfine interaction.

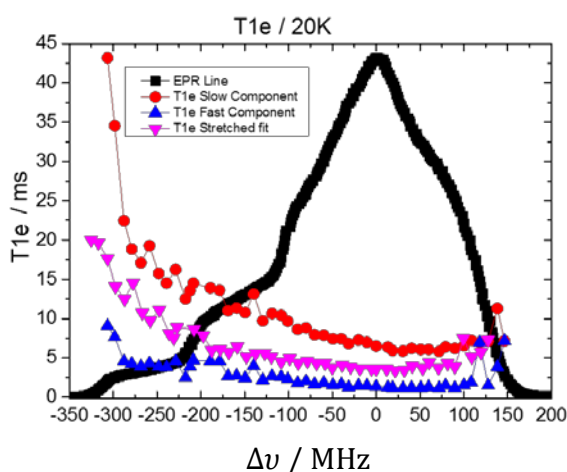


Figure 6. The frequency dependence of T_{1e} of 10 mM TEMPOL at 20 K, measured every 10 MHz . Each point corresponds to a measurement fitted with a bi-exponential fit as noted on the figure.

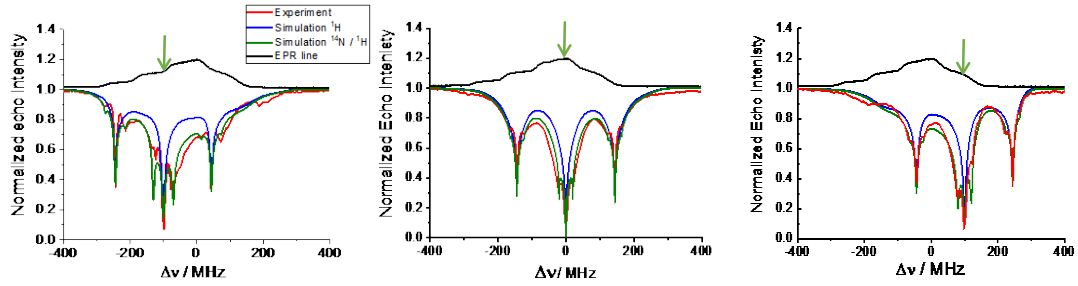


Figure 7. Experimental (red) and simulated (blue and green) ELDOR spectra of 10 mM TEMPOL at different positions along the EPR spectrum (in black) measured at 20 K. The green arrow indicates $\Delta\nu_{\text{det}}$. All spectra were fitted with $\Lambda^{eSD} = 60 \mu\text{s}^{-3}$, $T_{1e} = 5.7 \text{ ms}$, $T_2 = 100 \mu\text{s}$. The blue spectra show the result of the simulation including only the ^1H while the green spectra include both ^1H and ^{14}N SE contributions. The detection frequency is marked with a green arrow at the top of each panel. The simulation was performed using 350 frequency bins with a 2 MHz width, spanning the whole EPR spectrum. The pump frequency spanned 1000 MHz with steps of 2 MHz, the forbidden transition fitting parameters were: $A_H^{SE} = 3 \cdot 10^{-3}$, $A_N^{SE} = 1.5 \cdot 10^{-3}$, $A_{HN}^{SE} = 0.4 \cdot 10^{-3}$. The NMR frequencies (corresponding the ν_k in Eq. 12) used in the simulation were $\nu_{H_NMR} = \pm 144 \text{ MHz}$, $\nu_{N_NMR} = \pm 20 \text{ MHz}$ for ^{14}N , and $\nu_{HN_NMR} = \nu_H \pm 20 \text{ MHz}$ for the ^1H and ^{14}N combinations.

1 To examine the degree of the influence of the ^{14}N SE on the electron depolarization at
 2 higher radical concentrations, where the ELDOR spectrum is shaped primarily by the
 3 eSD process, we tested also the 20 mM sample and used the eSD model to simulate the
 4 ELDOR lineshape recorded with ν_{det} set to the center of the EPR spectrum, as shown
 5 in Figure 8. Because of the high electron spin concentration, the eSD causes large
 6 depolarization of the EPR spectrum, which translates in extensive broadening of the
 7 ELDOR spectrum.

8 Figure 8 shows in red the experimental ELDOR spectrum, where although the lineshape
 9 of this spectrum is determined by the eSD process, we can still see small signals coming
 10 from the ^{14}N SE. Simulation including both the ^1H and ^{14}N SE with $\Lambda^{eSD} = 400 \mu\text{s}^{-3}$
 11 gave a good agreement with the experimental spectrum. In contrast, setting $\Lambda^{eSD} =$
 12 $400 \mu\text{s}^{-3}$ and taking into account only the contributions of the ^1H SE, did not result in a
 13 good fit. This shows that even at relative high radical concentrations, the effect of the

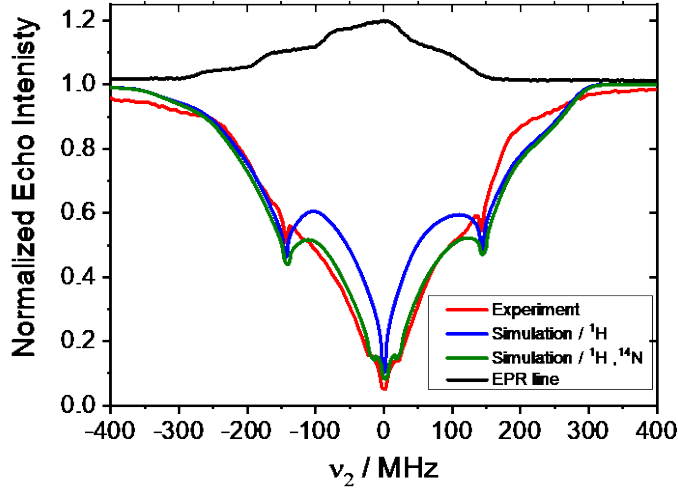


Figure 8. Experimental (red) and simulated (blue and green) ELDOR spectra of 20 mM TEMPOL recorded at the maximum of the EPR spectrum (shown in black). The fit was achieved with $A^{eSD} = 400 \mu\text{s}$, ${}^{-3}T_{1e} = 5.7 \text{ ms}$, $T_2 = 100 \mu\text{s}$. The blue spectra show the result of the simulation including only the ${}^1\text{H}$ while the green spectra include both ${}^1\text{H}$ and ${}^{14}\text{N}$ SE contributions. The forbidden transition fitting parameters were: $A_H^{SE} = 3 \cdot 10^{-3}$, $A_N^{SE} = 5 \cdot 10^{-3}$, $A_{HN}^{SE} = 0.4 \cdot 10^{-3}$ and the nuclear frequencies were the same as in Fig. 7.

1 depolarization due to the ${}^{14}\text{N}$ SE can still be significant and if not included can introduce
 2 inaccuracies in the eSD parameters and thus also in the DNP spectra, derived from the
 3 depolarized EPR lineshapes that are constructed using these parameters. Earlier
 4 measurements showed that 20 mM TEMPOL concentration, ELDOR spectra
 5 measured at the g_y and g_z position gave the same quality fit with the same A^{eSD} ,
 6 implying that at this concentration the relative contribution of the ${}^{14}\text{N}$ SE mechanism is
 7 small and can be accounted for by the simple model presented in this work.

8 **5 Conclusions**

9

10 In this work we use ELDOR measurements to determine the contributions of the ${}^{14}\text{N}$
 11 SE to the depolarization gradient within the EPR spectrum of TEMPOL during long
 12 MW irradiation, as commonly used in DNP measurements. For a low concentration
 13 (0.5 mM) TEMPOL sample, where the SE dominates and eSD is negligible, we have
 14 successfully reproduced all the SE related depolarization signals, including those
 15 involving combinations of ${}^1\text{H}$ - ${}^{14}\text{N}$ associated forbidden EPR transitions and those
 16 arising from off-resonance effects. Subsequently, we used the eSD model (Hovav et al.,

1 2015c) to simulate ELDOR spectra of 10 and 20 mM TEMPOL samples with ad-hoc
2 addition of electron depolarization due to the ^{14}N SE based on the frequencies
3 determined from the 0.5 mM sample. We observed that simulations including the ^{14}N
4 SE improved the fit with experimental ELDOR spectra for the 10 mM sample. However
5 we noticed that at the g_z region of the EPR spectrum the fit was not as good, indicating
6 that the model does not account sufficiently well for the large ^{14}N SE contributions
7 in this region. For the 20 mM concentration the model works well and the ^{14}N SE effect
8 is still significant and can affect the best fitted value of Λ^{eSD} . We conclude that
9 including ^{14}N SE in the eSD model is essential for obtaining reliable fitting at high
10 radical concentrations.

11

12 Acknowledgments

13 This work is supported by a grant of the Binational Science Foundation (Grant #2014149)
14 and was made possible in part by the historic generosity of the Harold Perlman Family (D.
15 G.). D. G. holds the Erich Klieger Professorial Chair in Chemical Physics.

16

17 **References**

- 18 Abragam, A.: Principles of nuclear magnetism, Clarendon Press, Oxford, Oxford., 1961.
- 19 Aliabadi, A., Zaripov, R., Salikhov, K., Voronkova, V., Vavilova, E., Abdulmalic, M. A., Ruffer,
20 T., Büchner, B. and Kataev, V.: Electron Spin Density on the N-Donor Atoms of Cu(II)-
21 (Bis)oxamidato Complexes As Probed by a Pulse ELDOR Detected NMR, J. Phys. Chem. B,
22 119(43), 13762–13770, doi:10.1021/acs.jpcc.5b03987, 2015.
- 23 de Boer, W.: Dynamic orientation of nuclei at low temperatures, J. Low Temp. Phys., 22(1–
24 2), 185–212, doi:10.1007/BF00655221, 1976.
- 25 Borghini, M.: Spin-Temperature Model of Nuclear Dynamic Polarization Using Free Radicals,
26 Phys. Rev. Lett., 20(9), 419–421, doi:10.1103/PhysRevLett.20.419, 1968.
- 27 Caracciolo, F., Filibian, M., Carretta, P., Rosso, A. and De Luca, A.: Evidence of spin-
28 temperature in dynamic nuclear polarization: An exact computation of the EPR spectrum,
29 Phys. Chem. Chem. Phys., 18(36), 25655–25662, doi:10.1039/c6cp05047f, 2016.
- 30 Cox, N., Lubitz, W. and Savitsky, A.: W band ELDOR detected NMR (EDNMR) spectroscopy as
31 a versatile technique for the characterisation of transition metal ligand interactions, Mol.
32 Phys., 111(18–19), 2788–2808, doi:10.1080/00268976.2013.830783, 2013.
- 33 Cox, N., Nalepa, A., Lubitz, W. and Savitsky, A.: ELDOR-detected NMR: A general and robust

1 method for electron-nuclear hyperfine spectroscopy?, *J. Magn. Reson.*, 280, 63–78,
2 doi:10.1016/j.jmr.2017.04.006, 2017.

3 Florent, M., Kaminker, I., Nagarajan, V. and Goldfarb, D.: Determination of the ^{14}N
4 quadrupole coupling constant of nitroxide spin probes by W-band ELDOR-detected NMR, *J.*
5 *Magn. Reson.*, 210(2), 192–199, doi:10.1016/j.jmr.2011.03.005, 2011.

6 Goldfarb, D., Lipkin, Y., Potapov, A., Gorodetsky, Y., Epel, B., Raitsimring, A. M., Radoul, M.
7 and Kaminker, I.: HYSORE and DEER with an upgraded 95GHz pulse EPR spectrometer., *J.*
8 *Magn. Reson.*, 194(1), 8–15, doi:10.1016/j.jmr.2008.05.019, 2008.

9 Goldman, M.: Spin temperature and magnetic resonance in solids, edited by (Oxford Univ.
10 Press, London., 1970.

11 Harris, T., Bretschneider, C. and Frydman, L.: Dissolution DNP NMR with solvent mixtures:
12 Substrate concentration and radical extraction, *J. Magn. Reson.*, 211(1), 96–100,
13 doi:10.1016/j.jmr.2011.04.001, 2011.

14 Hovav, Y., Feintuch, A. and Vega, S.: Theoretical aspects of dynamic nuclear polarization in
15 the solid state - the solid effect., *J. Magn. Reson.*, 207(2), 176–189,
16 doi:10.1016/j.jmr.2010.10.016, 2010.

17 Hovav, Y., Shimon, D., Kaminker, I., Feintuch, A., Goldfarb, D. and Vega, S.: Effects of the
18 electron polarization on dynamic nuclear polarization in solids, *Phys. Chem. Chem. Phys.*,
19 17(8), 6053–6065, doi:10.1039/C4CP05625F, 2015a.

20 Hovav, Y., Kaminker, I., Shimon, D., Feintuch, A., Goldfarb, D. and Vega, S.: The electron
21 depolarization during dynamic nuclear polarization: Measurements and simulations, *Phys.*
22 *Chem. Chem. Phys.*, 17(1), 226–244, doi:10.1039/c4cp03825h, 2015b.

23 Hovav, Y., Kaminker, I., Shimon, D., Feintuch, A., Goldfarb, D. and Vega, S.: The electron
24 depolarization during dynamic nuclear polarization: Measurements and simulations, *Phys.*
25 *Chem. Chem. Phys.*, 17(1), 226–244, doi:10.1039/c4cp03825h, 2015c.

26 Hwang, C. F. and Hill, D. A.: New Effect in Dynamic Polarization, *Phys. Rev. Lett.*, 18(4), 110–
27 112, doi:10.1103/PhysRevLett.18.110, 1967.

28 Jeschke, G. and Spiess, H. W.: NMR-correlated high-field electron paramagnetic resonance
29 spectroscopy, *Chem. Phys. Lett.*, 293(August), 9–18, 1998.

30 Kaminker, I., Wilson, T. D., Savelieff, M. G., Hovav, Y., Zimmermann, H., Lu, Y. and Goldfarb,
31 D.: Correlating nuclear frequencies by two-dimensional ELDOR-detected NMR spectroscopy.,
32 *J. Magn. Reson.*, 240, 77–89, doi:10.1016/j.jmr.2013.12.016, 2014.

33 Kessenikh, A. V., Manenkov, A. A. and G.I., P.: On explanation of experimental data on
34 dynamic polarization of protons in irradiated polyethylenes, *Sov. Physics-Solid State*, 6(3),
35 641–643, 1964.

36 Kundu, K., Feintuch, A. and Vega, S.: Electron-Electron Cross-Relaxation and Spectral
37 Diffusion during Dynamic Nuclear Polarization Experiments on Solids, *J. Phys. Chem. Lett.*,
38 9(7), 1793–1802, doi:10.1021/acs.jpcllett.8b00090, 2018a.

39 Kundu, K., Ramirez-Cohen, M., Feintuch, A., Goldfarb, D. and Vega, S.: Experimental
40 Quantification of Electron Spectral-Diffusion under static DNP conditions, *Phys. Chem.*
41 *Chem. Phys.*, 478–489, doi:10.1039/C8CP05930F, 2018b.

- 1 Leavesley, A., Shimon, D., Siaw, T. A., Feintuch, A., Goldfarb, D., Vega, S., Kaminker, I. and
2 Han, S.: Effect of electron spectral diffusion on static dynamic nuclear polarization at 7 Tesla,
3 *Phys. Chem. Chem. Phys.*, 19(5), 3596–3605, doi:10.1039/c6cp06893f, 2017.
- 4 Leavesley, A., Jain, S., Kamniker, I., Zhang, H., Rajca, S., Rajca, A. and Han, S.: Maximizing
5 NMR signal per unit time by facilitating the e-e-n cross effect DNP rate, *Phys. Chem. Chem.*
6 *Phys.*, 20(43), 27646–27657, doi:10.1039/c8cp04909b, 2018.
- 7 Mentink-Vigier, F., Collauto, A., Feintuch, A., Kaminker, I., Tarle, V. and Goldfarb, D.:
8 Increasing sensitivity of pulse EPR experiments using echo train detection schemes, *J. Magn.*
9 *Reson.*, 236, 117–125, doi:10.1016/j.jmr.2013.08.012, 2013.
- 10 Nalepa, A., Möbius, K., Lubitz, W. and Savitsky, A.: High-field ELDOR-detected NMR study of
11 a nitroxide radical in disordered solids: Towards characterization of heterogeneity of
12 microenvironments in spin-labeled systems, Elsevier Inc., 2014.
- 13 Nalepa, A., Möbius, K., Plato, M., Lubitz, W. and Savitsky, A.: Nitroxide Spin Labels—
14 Magnetic Parameters and Hydrogen-Bond Formation: A High-Field EPR and EDNMR Study,
15 *Appl. Magn. Reson.*, (0123456789), doi:10.1007/s00723-018-1073-3, 2018.
- 16 Provotorov, B. N.: Magnetic resonance saturation in crystals, *Sov. Phys. JETP*, 14(5), 1126–
17 1131, 1962.
- 18 Ramirez Cohen, M., Mendelman, N., Radoul, M., Wilson, T. D., Savelieff, M. G.,
19 Zimmermann, H., Kaminker, I., Feintuch, A., Lu, Y. and Goldfarb, D.: Thiolate Spin Population
20 of Type I Copper in Azurin Derived from 33 S Hyperfine Coupling, *Inorg. Chem.*, 56(11),
21 6163–6174, doi:10.1021/acs.inorgchem.7b00167, 2017.
- 22 Rapatskiy, L., Cox, N., Savitsky, A., Ames, W. M., Sander, J., Nowaczyk, M. M., Rögner, M.,
23 Boussac, A., Neese, F., Messinger, J. and Lubitz, W.: Detection of the water-binding sites of
24 the oxygen-evolving complex of photosystem II using W-band 17O electron-electron double
25 resonance-detected NMR spectroscopy, *J. Am. Chem. Soc.*, 134(40), 16619–16634,
26 doi:10.1021/ja3053267, 2012.
- 27 Schweiger, A. and Jeschke, G.: Principles of Pulse Electron Paramagnetic Resonance, Oxford
28 University Press., 2001.
- 29 Shimon, D., Hovav, Y., Feintuch, A., Goldfarb, D. and Vega, S.: Dynamic Nuclear Polarization
30 in the solid state: a transition between the cross effect and the solid effect., *Phys. Chem.*
31 *Chem. Phys.*, 14(16), 5729–43, doi:10.1039/c2cp23915a, 2012.
- 32 Shimon, D., Feintuch, A., Goldfarb, D. and Vega, S.: Static (1)H dynamic nuclear polarization
33 with the biradical TOTAPOL: a transition between the solid effect and the cross effect., *Phys.*
34 *Chem. Chem. Phys.*, 16(14), 6687–6699, doi:10.1039/c3cp55504f, 2014.
- 35 Siaw, T. A., Fehr, M., Lund, A., Latimer, A., Walker, S. A., Edwards, D. T. and Han, S. I.: Effect
36 of electron spin dynamics on solid-state dynamic nuclear polarization performance, *Phys.*
37 *Chem. Chem. Phys.*, 16(35), 18694–18706, doi:10.1039/c4cp02013h, 2014.
- 38 Stoll, S. and Schweiger, A.: EasySpin, a comprehensive software package for spectral
39 simulation and analysis in EPR., *J. Magn. Reson.*, 178(1), 42–55,
40 doi:10.1016/j.jmr.2005.08.013, 2006.
- 41 Tan, K. O., Yang, C., Weber, R. T., Mathies, G. and Griffin, R. G.: Time-optimized pulsed
42 dynamic nuclear polarization, *Sci. Adv.*, 5(1), 1–8, doi:10.1126/sciadv.aav6909, 2019.

1 Thankamony, A. S. L., Wittmann, J. J., Kaushik, M. and Corzilius, B.: Dynamic nuclear
2 polarization for sensitivity enhancement in modern solid-state NMR, *Prog. Nucl. Magn.*
3 *Reson. Spectrosc.*, 102–103, 120–195, doi:10.1016/j.pnmrs.2017.06.002, 2017.

4 Wang, X., McKay, J. E., Lama, B., Van Tol, J., Li, T., Kirkpatrick, K., Gan, Z., Hill, S., Long, J. R.
5 and Dorn, H. C.: Gadolinium based endohedral metallofullerene Gd₂@C₇₉N as a relaxation
6 boosting agent for dissolution DNP at high fields, *Chem. Commun.*, 54(19), 2425–2428,
7 doi:10.1039/c7cc09765d, 2018.

8 Weber, E. M. M., Vezin, H., Kempf, J. G., Bodenhausen, G., Abergél, D. and Kurzbach, D.:
9 Anisotropic longitudinal electronic relaxation affects DNP at cryogenic temperatures, *Phys.*
10 *Chem. Chem. Phys.*, 19(24), 16087–16094, doi:10.1039/c7cp03242k, 2017.

11 Wenckebach, T.: *Essentials of Dynamic Nuclear Polarization*, Spindrift Publications., 2016.

12 Wili, N. and Jeschke, G.: Chirp echo Fourier transform EPR-detected NMR, *J. Magn. Reson.*,
13 289, 26–34, doi:10.1016/j.jmr.2018.02.001, 2018.

14 Wollan, D. S.: Dynamic Nuclear Polarization with an inhomogeneously broadened ESR line.
15 I. Theory, *Phys. Rev. B*, 13(9), 1976.

16

17

18

19